magnetochemistry

MDPI

Supplementary Material: New Cyanido-Bridged Heterometallic 3d-4f 1D Coordination Polymers: Synthesis, Crystal Structures and Magnetic Properties

Diana Dragancea [1,2,*], Ghenadie Novitchi [3,*], Augustin M. Mădălan [1] and Marius Andruh [1,*]

[1] Inorganic Chemistry Laboratory, Faculty of Chemistry, University of Bucharest, Str. Dumbrava Rosie nr. 23, 020464 Bucharest, Romania; augustin.madalan@chimie.unibuc.ro
[2] Institute of Chemistry, Str. Academiei nr. 3, MD 2028 Chișinău, Republic of Moldova
[3] CNRS, University Grenoble Alpes, LNCMI, F-38000 Grenoble, France
* Correspondence: ddragancea@gmail.com (D.D.); ghenadie.novitchi@lncmi.cnrs.fr (G.N.); marius.andruh@dnt.ro (M.A.)

Table S1. Crystallographic data, details of data collection and structure refinement parameters of compounds 1-3.

Compound	**1_{GdFe}**	**2_{DyFe}**	**3_{DyCo}**
Formula	$C_{17}H_{21}FeGdN_{13}O_5$	$C_{17}H_{25}DyFeN_{13}O_7$	$C_{17}H_{21}DyCoN_{13}O_5$
M ($g \cdot mol^{-1}$)	700.57	741.85	708.90
Temperature (K)	293(2)	293(2)	293(2)
Wavelength (Å)	0.71073	0.71073	0.71073
Crystal system	orthorhombic	monoclinic	orthorhombic
Space group	P bca	$P2_1/c$	P bca
a (Å)	12.6342(5)	12.7058(3)	12.5194(2)
b (Å)	17.1373(8)	12.6290(3	17.1163(3)
c (Å)	24.4164(9)	17.2547(4)	24.2330(5)
α (°)	90	90	90
β (°)	90	103.466(2)	90
γ (°)	90	90	90
V ($Å^3$)	5286.5(4)	2692.60(11)	5192.79(16)
Z	8	4	8
D_c ($g \cdot cm^{-3}$)	1.760	1.835	1.814
μ (mm^{-1})	3.089	3.357	3.549
F (0 0 0)	2752	1468	2776
Goodness-of-fit (GOF) on F^2	1.145	1.042	1.070
Final R_1, wR_2 [$I > 2\sigma(I)$]	0.0520, 0.1081	0.0189, 0.0439	0.0208, 0.0480
R_1, wR_2 (all data)	0.0612, 0.1115	0.0232, 0.0450	0.0250, 0.0494

Table S2. SHAPE measures of the 9-coordinate lanthanide polyhedra.

Shape[a,b]	**1_{GdFe}**	**2_{DyFe}**	**3_{DyCo}**
EP-9	31.303	31.929	31.460
OPY-9	22.837	23.736	22.899
HBPY-9	16.116	17.242	16.445
JTC-9	15.267	14.905	15.030
JCCU-9	7.501	8.256	7.596
CCU-9	6.428	7.159	6.527
JCSAPR-9	4.007	2.657	3.677
CSAPR-9	**2.888**	**1.841**	**2.677**
JTCTPR-9	3.222	2.456	2.962
TCTPR-9	2.989	1.944	2.691
JTDIC-9	12.885	12.794	12.980
HH-9	6.655	8.182	7.014
MFF-9	2.535	2.077	2.422

[a] Abbreviations: EP-9, enneagon; OPY-9, octagonal pyramid; HBPY-9, Heptagonal bipyramid; JTC-9, Johnson triangular cupola J3; JCCU-9, capped cube J8; CCU-9, spherical-relaxed capped cube; JCSAPR-9, capped square antiprism J10; CSAPR-9, spherical capped square antiprism; JTCTPR-9, tricapped trigonal prism J51; TCTPR-9, spherical tricapped trigonal prism; JTDIC-9, tridiminished icosahedron J63; HH-9, hula-hoop; MFF-9, muffin.

[b] The values in boldface indicate the closest polyhedron according to the Continuous Shape Measures

Table S3. Selected bond distances (Å) and angles (°) for compounds **1-3.**

$\mathbf{1}_{GdFe}$		$\mathbf{2}_{DyFe}$		$\mathbf{3}_{DyCo}$	
Gd1–O1	**2.423(5)**	**Dy1–O1**	2.3652(18)	Dy1–O1	2.398(2)
Gd1–O2	2.406(5)	Dy1–O2	2.3298(18)	Dy1–O2	2.382(2)
Gd1–O3	2.330(5)	Dy1–O3	2.3783(13)	Dy1–O3	2.308(2)
Gd1–O4	2.375(5)	Dy1–O4	2.3557(12)	Dy1–O4	2.3518(19)
Gd1–N3	2.598(6)	Dy1–N3	2.553(2)	Dy1–N3	2.574(2)
Gd1–N4	2.584(6)	Dy1–N4	2.503(2)	Dy1–N4	2.562(2)
Gd1–N5	2.592(6)	Dy1–N5	2.528(2)	Dy1–N5	2.567(2)
Gd1–N8	2.534(6)	Dy1–N8	2.556(2)	Dy1–N8	2.519(3)
Gd1–N13	2.566(6)	Dy1–N13	2.533(2)	Dy1–N13	2.544(3)
Fe1–C12	1.943(7)	Fe1–C12	1.957(3)	Co1–C12	1.898(3)
Fe1–C13	1.926(7)	Fe1–C13	1.945(3)	Co1–C13	1.886(3)
Fe1–C14	1.945(9)	Fe1–C14	1.943(3)	Co1–C14	1.908(3)
Fe1–C15	1.921(7)	Fe1–C15	1.948(3)	Co1–C15	1.898(3)
Fe1–C16	1.948(9)	Fe1–C16	1.929(3)	Co1–C16	1.905(3)
Fe1–C17	1.960(7)	Fe1–C17	1.949(3)	Co1–C17	1.915(3)
Gd1–C12–N8	154.4(5)	Dy1–C12–N8	159.2(2)	Dy1–C12–N8	155.3(2)
Gd1–C17–N13	158.5(6)	Dy1–C17–N13	154.3(2)	Dy1–C17–N13	159.0(2)
O1–Gd1–O2	102.03(17)	O1–Dy1–O2	96.21(7)	O1–Dy1–O2	100.18(7)
O1–Gd1–N3	62.37(17)	O1–Dy1–N3	63.57(7)	O1–Dy1–N3	62.91(7)
O2–Gd1–N5	62.80(18)	O2–Dy1–N5	64.18(7)	O2–Dy1–N5	63.27(7)
N3–Gd1–N4	60.77(19)	N3–Dy1–N4	61.66(7)	N3–Dy1–N4	61.12(8)
N5–Gd1–N4	60.41(19)	N5–Dy1–N4	61.92(7)	N5–Dy1–N4	60.94(8)
O4–Gd1–O3	121.2(2)	O4–Dy1–O3	129.69(6)	O4–Dy1–O3	123.11(9)
O1–Gd1–O4	69.35(16)	O1–Dy1–O4	72.64(5)	O1–Dy1–O4	69.17(7)
N8–Gd1–N13	74.31(19)	N8–Dy1–N13	74.54(7)	N8–Dy1–N13	74.96(8)

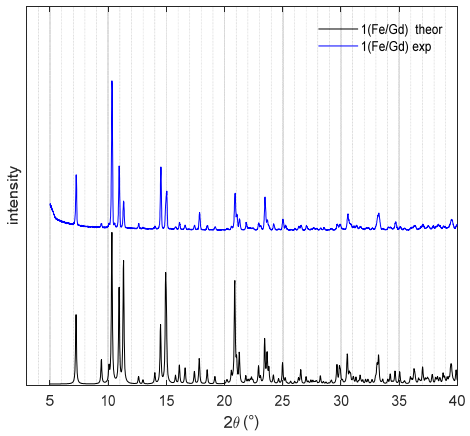

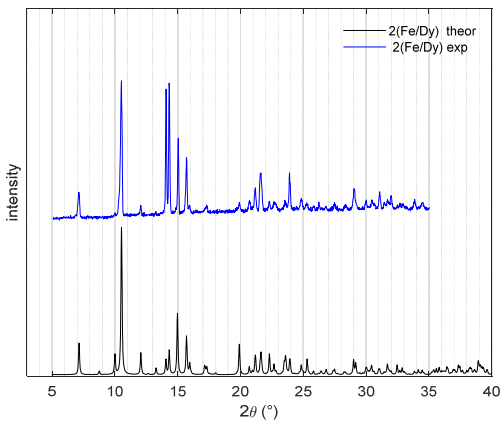

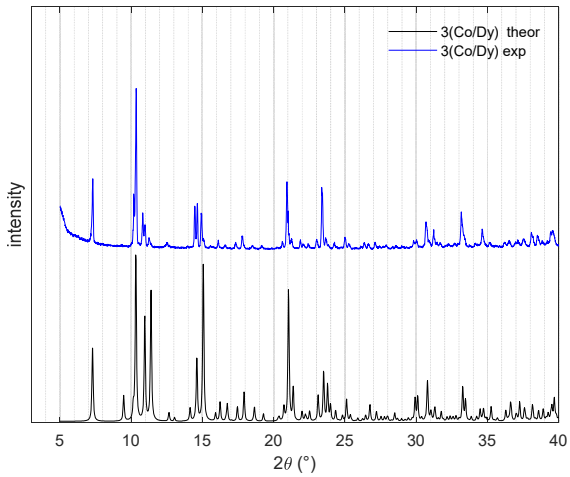

Figure S1. The experimental (blue) and simulated (black) powder X-ray diffraction patterns for **1**$_{GdFe,}$ **2**$_{DyFe}$**, 3**$_{DyCo.}$

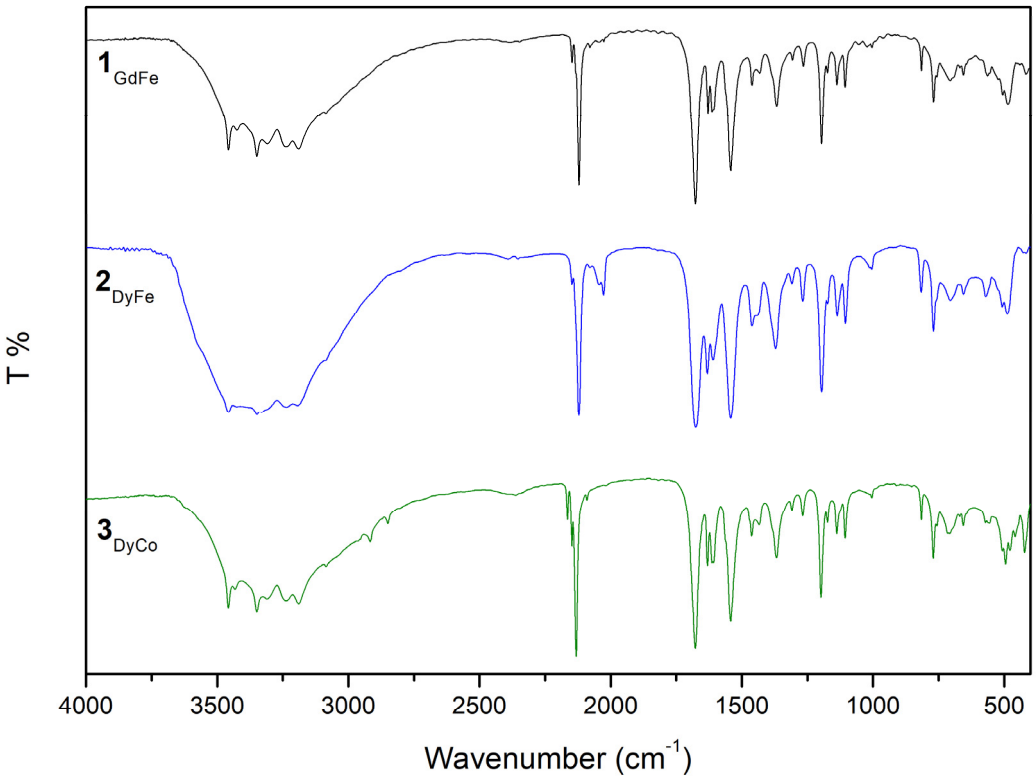

Figure S2. The FTIR spectra for **1**$_{GdFe}$, **2**$_{DyFe}$, **3**$_{DyCo}$.

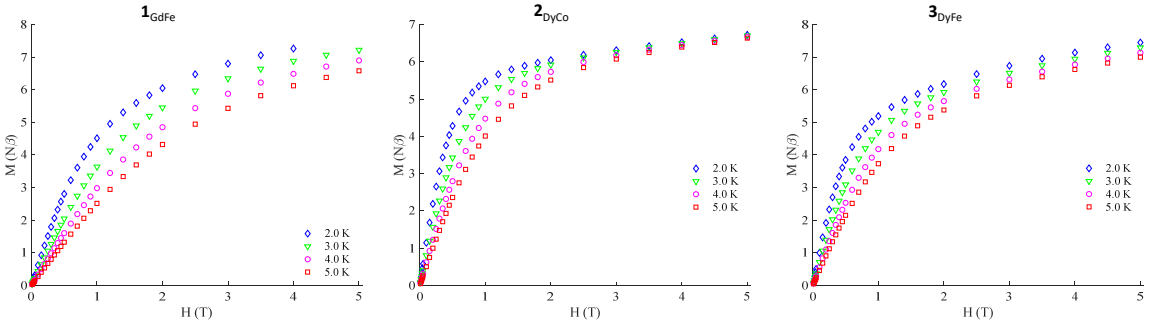

Figure S3. Isothermal magnetization (M) curves for complexes **1**$_{GdFe}$, **2**$_{DyFe}$, **3**$_{DyCo}$, and in the 2 to 5 K range.

Mathematical expressions for *ac* susceptibility given by the generalized Debye model for two relaxation processes:

$$\chi'(\omega) = \chi_{S,tot} + \Delta\chi_1 \frac{1+(\omega\tau_1)^{1-\alpha_1}\sin\left(\frac{\pi\alpha_1}{2}\right)}{1+(\omega\tau_1)^{1-\alpha_1}\sin\left(\frac{\pi\alpha_1}{2}\right)+(\omega\tau_1)^{(2-2\alpha_1)}} + \Delta\chi_2 \frac{1+(\omega\tau_2)^{1-\alpha_2}\sin\left(\frac{\pi\alpha_2}{2}\right)}{1+(\omega\tau_2)^{1-\alpha_2}\sin\left(\frac{\pi\alpha_2}{2}\right)+(\omega\tau_2)^{(2-2\alpha_2)}} \quad \text{(eq. S1)}$$

$$\chi''(\omega) = \Delta\chi_1 \frac{1+(\omega\tau_1)^{1-\alpha_1}\cos\left(\frac{\pi\alpha_1}{2}\right)}{1+(\omega\tau_1)^{1-\alpha_1}\sin\left(\frac{\pi\alpha_1}{2}\right)+(\omega\tau_1)^{(2-2\alpha_1)}} + \Delta\chi_2 \frac{1+(\omega\tau_2)^{1-\alpha_2}\cos\left(\frac{\pi\alpha_2}{2}\right)}{1+(\omega\tau_2)^{1-\alpha_2}\sin\left(\frac{\pi\alpha_2}{2}\right)+(\omega\tau_2)^{(2-2\alpha_2)}} \quad \text{(eq. S2)}$$

where $\omega = 2\pi\nu$

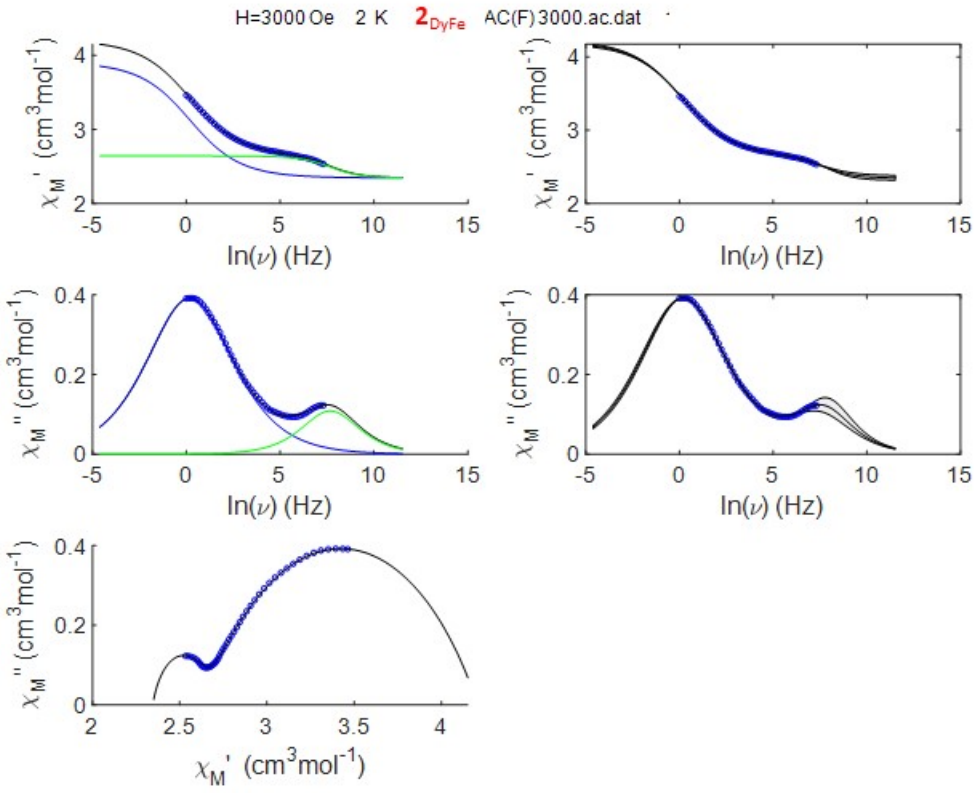

Figure S4. Example *ac* susceptibility analysis of frequency sweeping measurements for **2**$_{DyFe}$ using extended Debye model for two relaxation processes. (eq. S1, 2). The contribution of two-relaxation processes depicted in blue and green. The 95% confidence intervals depicted in the right in the gray color.

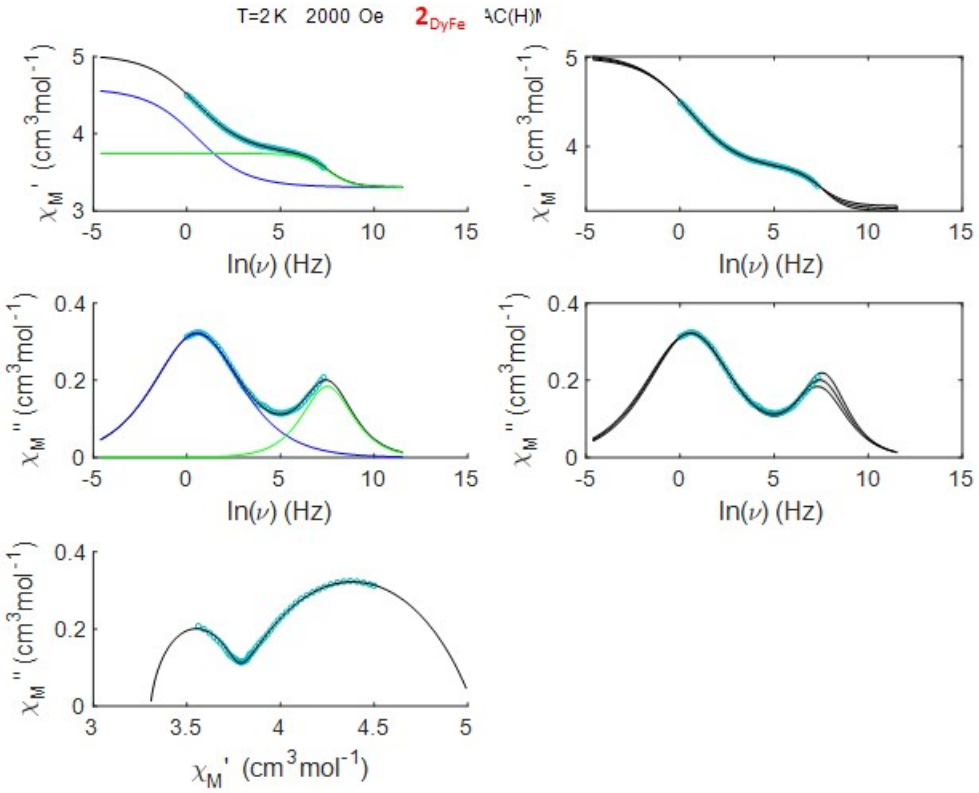

Figure S5. Example *ac* susceptibility analysis of field sweeping measurements for **2**$_{DyFe}$ using extended Debye model for two relaxation processes. (eq. S1, 2). The contribution of two-relaxation processes depicted in blue and green. The 95% confidence intervals depicted in the right in the gray color.

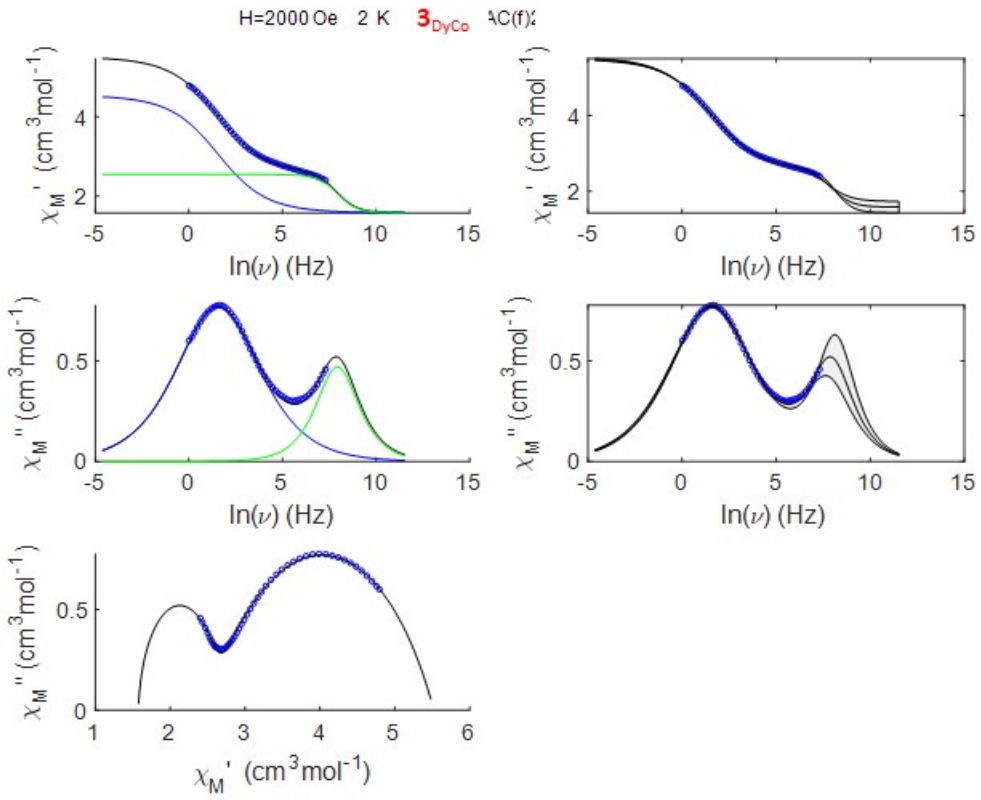

Figure S6. Example *ac* susceptibility analysis of frequency sweeping measurements for **3**$_{DyCo}$ using extended Debye model for two relaxation processes. (eq. S1, 2). The contribution of two-relaxation processes depicted in blue and green. The 95% confidence intervals depicted in the right in the gray color.

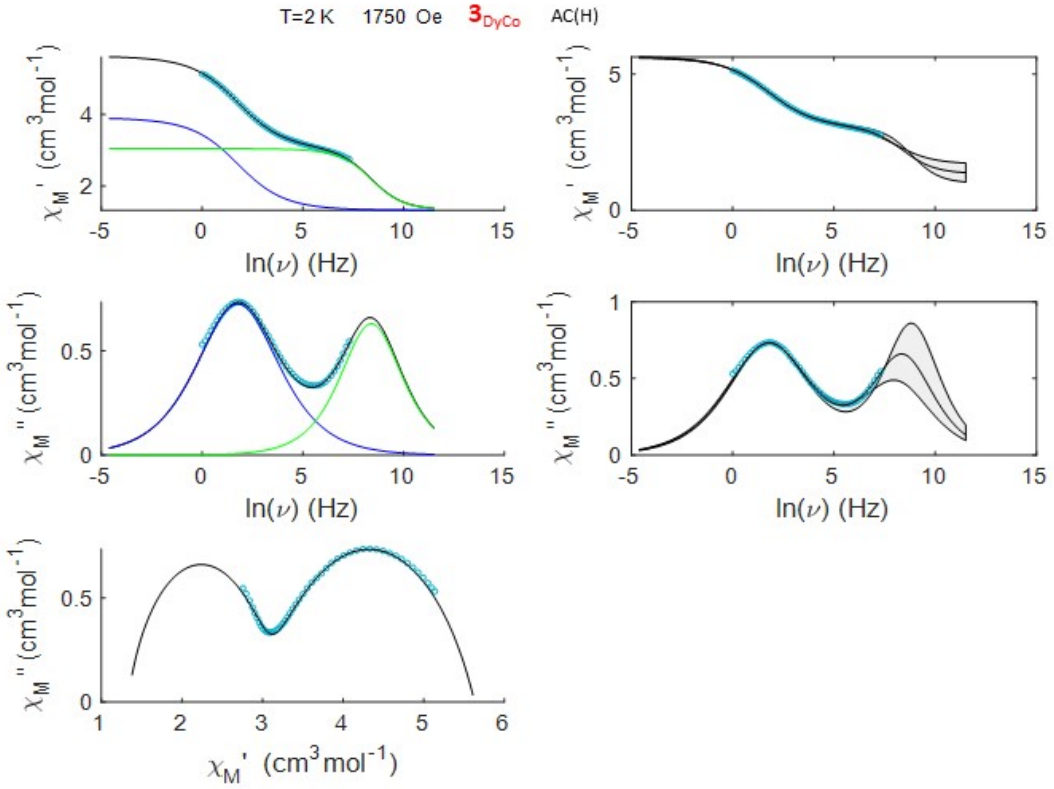

Figure S7. Example *ac* susceptibility analysis of field sweeping measurements for **3**$_{DyCo}$ using extended Debye model for two relaxation processes. (eq. S1, 2). The contribution of two-relaxation processes depicted in blue and green. The 95% confidence intervals depicted in the right in the gray color.

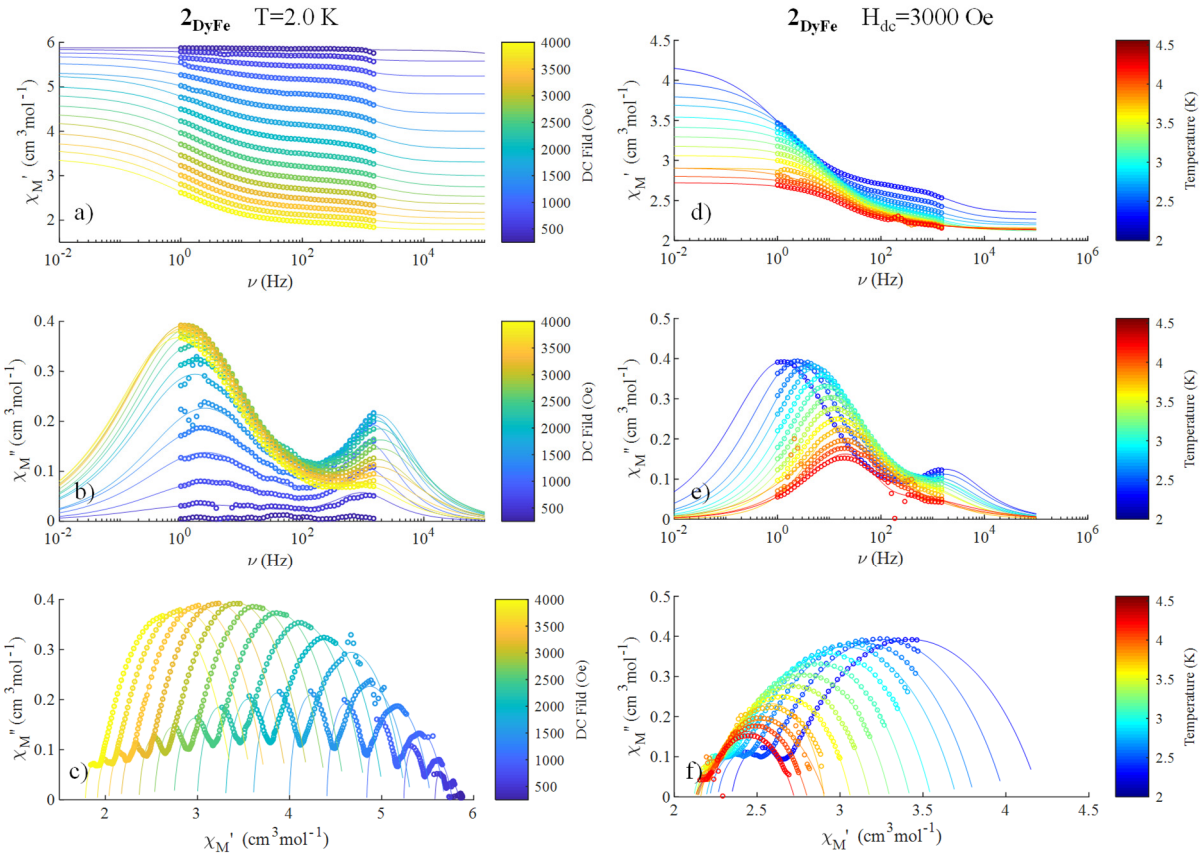

Figure S8. Field dependence (left) and temperature dependence (right) of *ac* susceptibility (H_{ac}=3.0 Oe) and Cole-Cole plots(c) and f)) for **2**$_{DyFe}$ at indicated temperatures and fields. The solid lines represented the best fits according the generalized Debye model for two relaxations process (eq. S1,2).

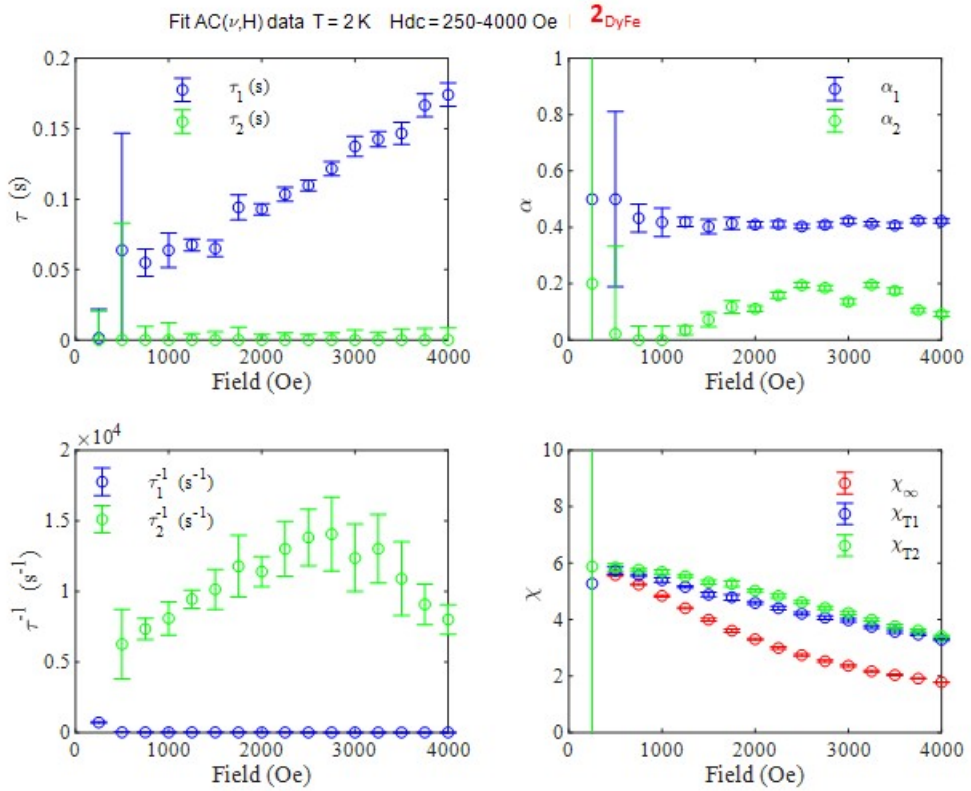

Figure S9. Graphical representation of variable parameters deduced from the best fits of the *ac* susceptibility of **2**$_{DyFe}$ collected with a 3.0 Oe *ac* field oscillating under different fields (see Figure 8 main text).

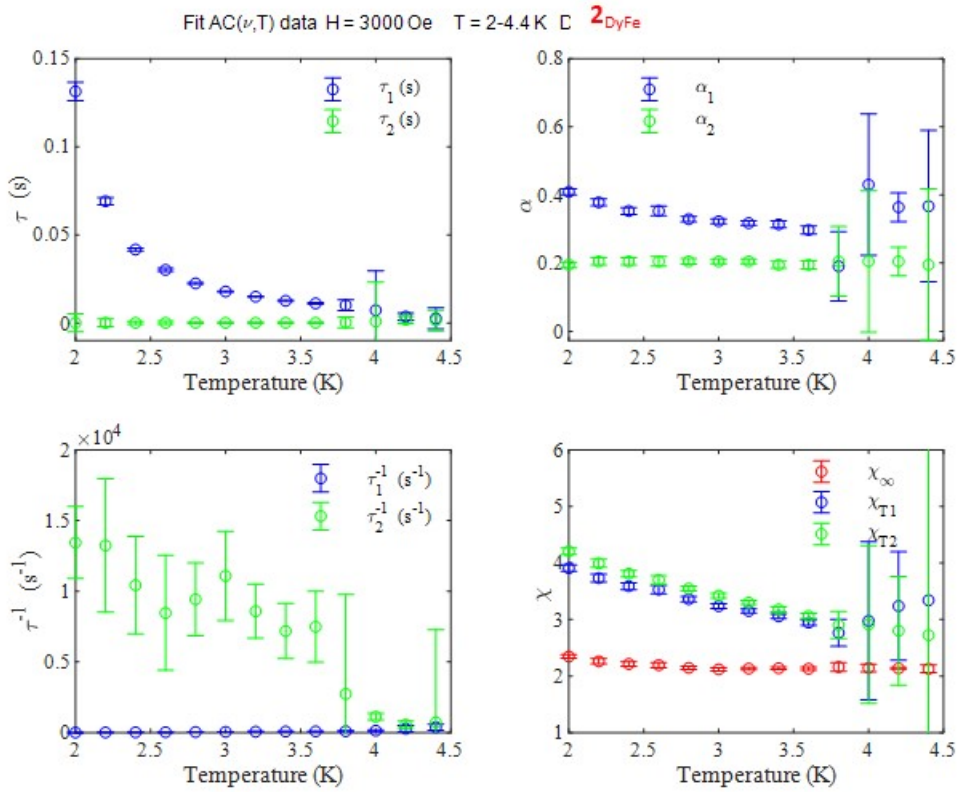

Figure S10. Graphical representation of variable parameters deduced from the best fits of the *ac* susceptibility of **2**$_{DyFe}$ collected with a 3.0 Oe *ac* field oscillating for deferent temperatures (see Figure 8 main text).

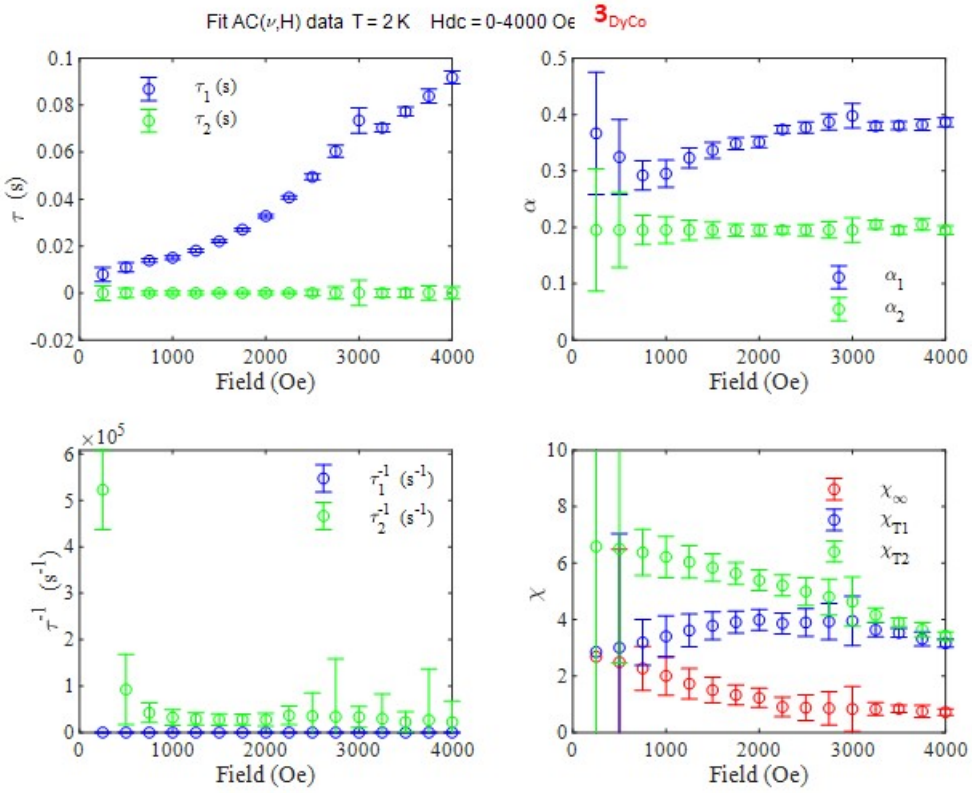

Figure S11. Graphical representation of variable parameters deduced from the best fits of the *ac* susceptibility of **3**$_{DyCo}$ collected with a 3.0 Oe *ac* field oscillating under different fields (see Figure 8 main text).

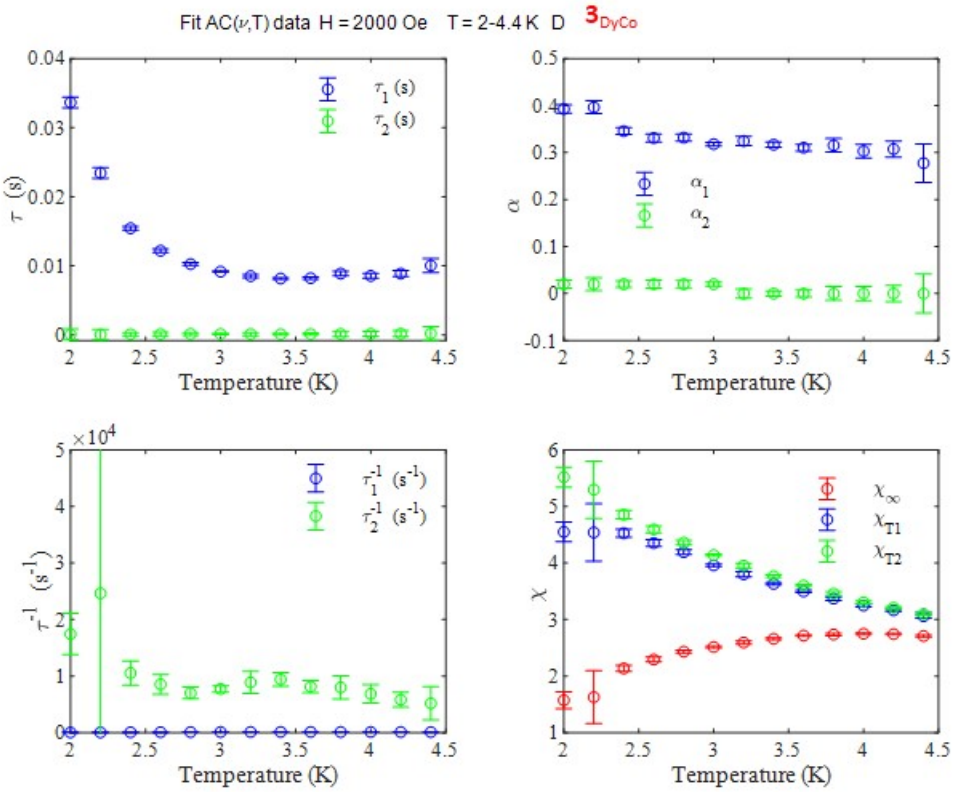

Figure S12. Graphical representation of variable parameters deduced from the best fits of the *ac* susceptibility of **3**$_{DyCo}$ collected with a 3.0 Oe *ac* field oscillating for deferent temperatures (see Figure 8 main text).

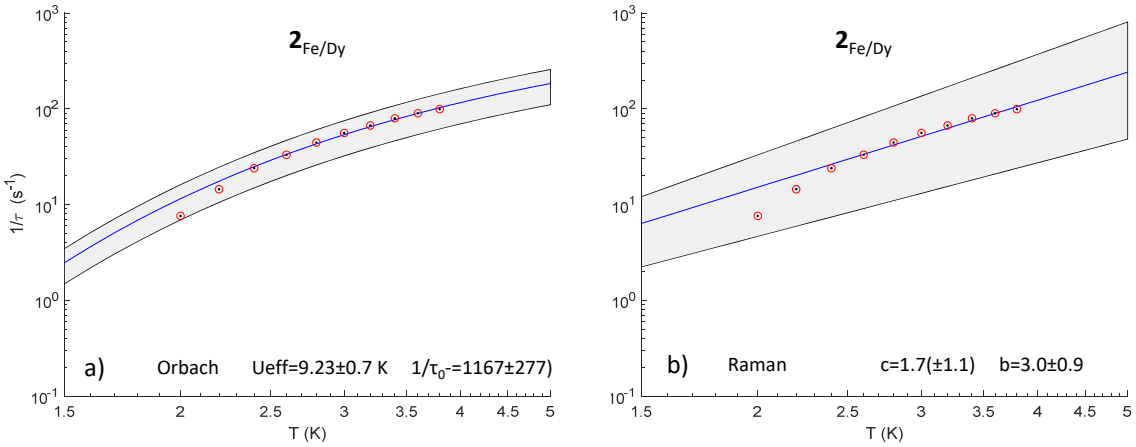

Figure S13. Temperature dependence of relaxation times for **2**$_{DyFe}$. The blues solid lines correspond to the fit for a) Orbach and b) Raman mechanisms of magnetic relaxation. The 95% confidence intervals are depicted on the right (gray color).

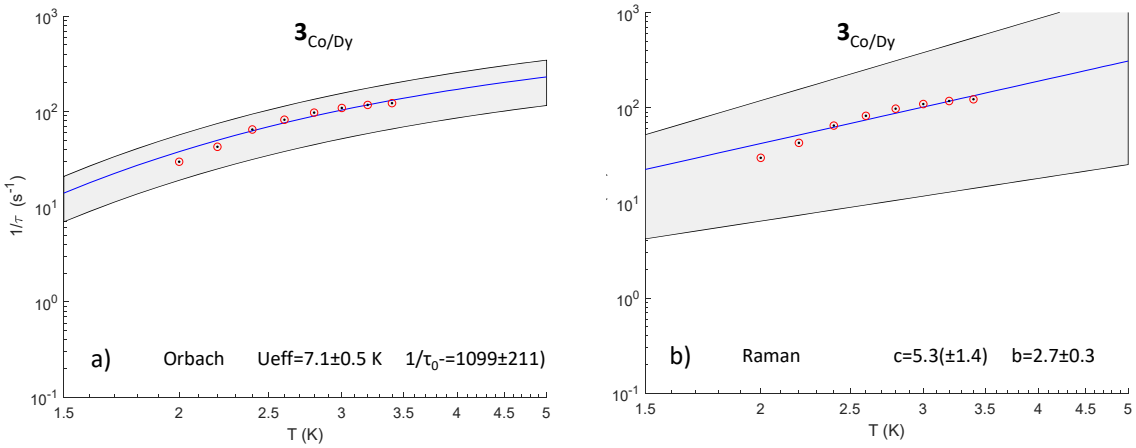

Figure S14. Temperature dependence of relaxation times for **3**$_{DyCo}$. The blues solid lines correspond to the fit for a) Orbach and b) Raman mechanisms of magnetic relaxation. The 95% confidence intervals are depicted on the right (gray color).

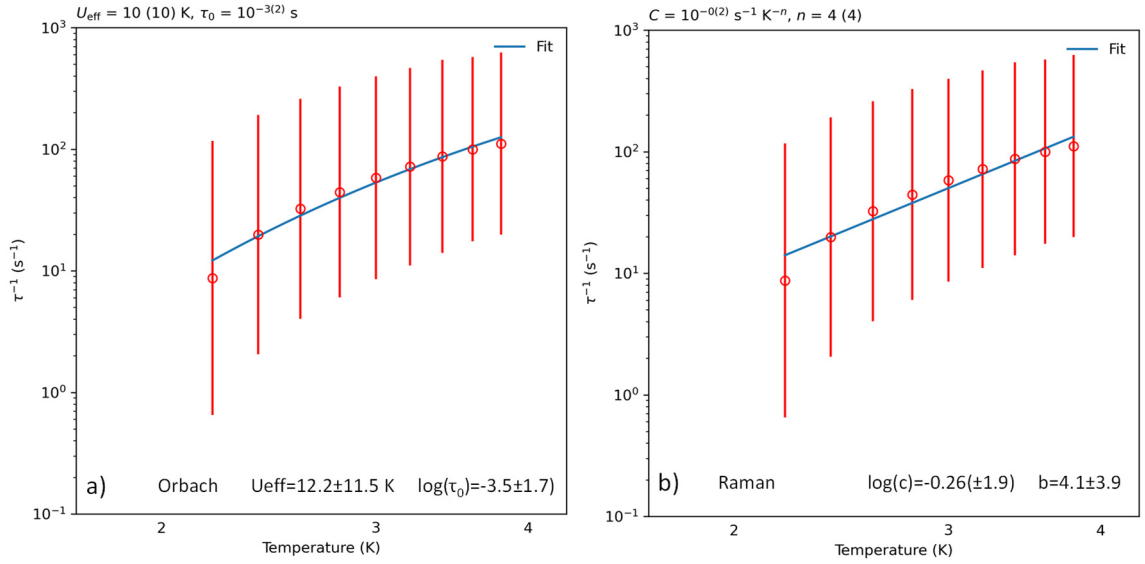

Figure S15. Temperature dependence of relaxation times for **2**$_{DyFe}$. The blues solid lines correspond to the fit for a) Orbach and b) Raman mechanisms of magnetic relaxation. Red line are error bars generated by *CC-FIT2 software [ref. Phys. Chem. Chem. Phys., 2019,21, 23567-23575].*